WP3000 Scatterometry

Objectives and relation to the Wavemill overall project

From field experiments, high correlation are found between local cross section signals and Doppler signals. Translated to satellite observations, this correlation, mainly explained by the correlation between tilting and orbital motions, leads to overall detectable Doppler biases. Contrary to HF radar systems, satellite radar measurements cannot distinguish a precise Bragg scatter, and the overall Doppler bias is driven by a wider spatial range mostly dominated by intermediate scale waves related to the tail of the wind wave spectrum and further depend upon the geometry of observations.

Accordingly, direct surface current retrieval from Doppler analysis is, for most environmental conditions, not possible. Corrections must be performed to compensate the residual Doppler bias associated to detected wind induced surface motions. These corrections will, to first order be wind amplitude and direction dependent.

Extracting the local wind speed and direction shall thus be essential to retrieve the residual Doppler associated to surface current.

It is also strongly emphasized that Wavemill should be, theoretically, the only existing or foreseen instrument which has the capability to consistently estimate the wind vector field at very high resolution (better than the km-scale).

The main goal of this WP is thus to study the feasibility to retrieve estimates of the surface wind vector and their associated Doppler shift contributions from Wavemill measurements (normalized radar cross section (NRCS) measurements and total Doppler), or in combination with first guess ancillary information (e.g, atmospheric model, scatterometer estimates, tide model, altimeter anomalies, ...).

Recommendations and rules will then be provided to propose strategies to best estimate the residual Doppler and the desired associated surface current.

3.1 Review of the scatterometer systems and foreseen limitations for Wavemill (WP3100)

3.1.1 Review of the scatterometer systems

A review of techniques to retrieve wind field from radar systems can be found in Portabella (2002) or Robinson (2004). The key considerations of this Scatterometry task is to understand the differences between standard systems (previous and actual) and Wavemill that impact the wind vector retrieval. For instance, WaveMill will operate at a different wavelength to existing C-band scatterometers, previously operated by ESA and presently available and operated by EUMETSAT. The implications of Ku-band operations, such as for the Nasa SCATterometer (NSCAT) system will then be discussed. The NSCAT configuration partly encompasses the Wavemill viewing geometry, and operated at both VV and HH polarization. We will take advantage of this past experience and the NSCAT data and associated geophysical model function will then be mainly used as reference throughout the study. The TRMM Ku-band data shall also be used to complete NSCAT data at very

low incidence angle.
Scatterometers use different techniques to collect measurements at multiple incident and azimuth angles. The figure 1 illustrates the NSCAT geometry using a fan-beam approach with 3 fixed antennas on each side of the subsatellite track. As for all scatterometer systems using fixed antennas (Seasat, ERS, NSCAT, ASCAT, Envisat, ….) , the part of the ground swath close to the nadir (350-km wide for NSCAT) is not observed and measurements cover an incidence angle ranging from ~ 18 degrees to ~ 58 degrees at far swath. Other existing techniques use Ku-band rotating antennas, either scanning fanbeam (the RFSCAT concept proposed for CFOSAT, Lin et al., 2000) or conically scanning pencil-beam (SeaWinds onboard QuikScat and OSCAT), to cover a complete swath including nadir-viewing. A pencil-beam scatterometer has several key advantages over a fan-beam scatterometer: it has a higher signal-to-noise ratio, is smaller in size, and it provides superior coverage. For that rotating systems, Ku-band operations are then preferred because it implies smaller antennas, but the rain contamination is a big concern by comparison with lower-frequency systems. An important advantage of the SeaWinds concept is that it performs measurements at a limited range of relatively high incidence angles (2 fixed incidence angles for QuikScat at 46° (H-pol.) and 54° (V-pol.)). This is a range where the NRCS sensitivity to wind vector is higher, by comparison with lower incidence angles, and it implies simpler geophysical model function (GMF). Accurate GMF calibration is mandatory for any system and it is simpler to attain it at fixed incidence angles. **Low incidence angles of the Wavemill system shall be one of the important concern.**
One another important characteristic of a scatterometer system is the azimuthal diversity for a given target (the ground resolution cell for wind vector estimation). The azimuthal diversity varies a lot across track for a rotating system which presents another challenge for the wind inversion. For the QuikScat case, azimuthal diversity is poor near the satellite nadir and in the far part of the swath leading to poorer wind retrieval statistics. For the Wavemill configuration using fixed antennas, we have to refer to past and existing fixed antennas systems using either 1 antenna (SAR systems), two orthogonal antennas (SASS onboard SeaSat) or three antennas (past and current scatterometers: ERS, NSCAT, ASCAT). The third antenna was decided to help resolve the ambiguity in the four equally probable wind directions obtained with a two orthogonal antennas system, leaving a 180° ambiguity in wind direction. For wind vector estimation, the ASCAT three-antenna system is now the reference operational system in Europe. Azimuthal diversity shall be a challenge for a Wavemill concept. With the added information on Doppler shift, it is anticipated that this additional “signed” information should help resolve the 180° ambiguity in wind direction.

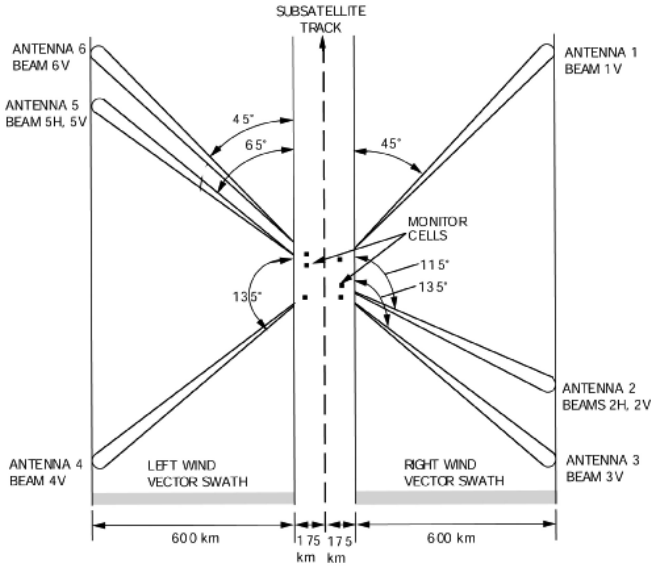

Figure 1: NSCAT scatterometer geometry

3.1.2 Foreseen limitations for Wavemill scatterometry

Considering imaging incidence angles between 10° and 22°, this is significantly steeper viewing geometry than most other scatterometers (which would typically operate between 20° and 55°). The implications will thus require consideration from both an instrument and a science perspective. To this end, analysis performed with the TRMM Precipitation Radar (PR), scanning between 0° and 18°, is used (Tran and Chapron, 2006, Tran et al., 2007), in complement to the NSCAT data covering incidence angles larger than 18°. As understood, limited sensitivity to wind speed and direction are expected around 10° to 12° incidence, with non negligible sea state dependency.
To illustrate such limitations, the Geophysical Model Function (GMF) developed for the Ku-band scatterometer NSCAT, operating at incidence angles ranging from 18° to 55°, is used to characterize the errors associated with winds derived solely from radar cross sections and the Javelin geometry.
The Ku-band NSCAT GMF (Wentz and Smith, 1999, Wentz and Freilich, 1998, Quilfen et al., 1999), hereafter Kmod, is expressed as the following three-term Fourier development:

$$NRCS=\sigma_{0P}=A_{0P}\left(1+A_{1P}\cos\Phi+A_{2P}\cos 2\Phi\right) \qquad (1)$$

where Φ is the wind direction relative to the antenna look direction and the A coefficients depend upon polarization, wind speed, and incidence angle.
The figure 2 presents the data obtained from TRMM and NSCAT missions to show the general behavior of Ku-band NRCS and the coherency over the nadir to off-nadir incidence angle range. As shown in natural units (Figure 2, top), the NRCS decreases sharply from nadir-viewing to about 10 ° of incidence angle. In this range the NRCS monotonically decreases with wind speed while it is monotonically increasing with wind speed beyond 10° of incidence angle (Figure 2, bottom). It has thus very little sensitivity to wind speed near 10° of incidence angle. The NRCS wind speed dependency is given by the A_{0P} term in equation (1). The Figure 3 presents its behavior at VV and HH polarization for 18°, thus close to the Wavemill configuration, and at 48° of incidence angle.

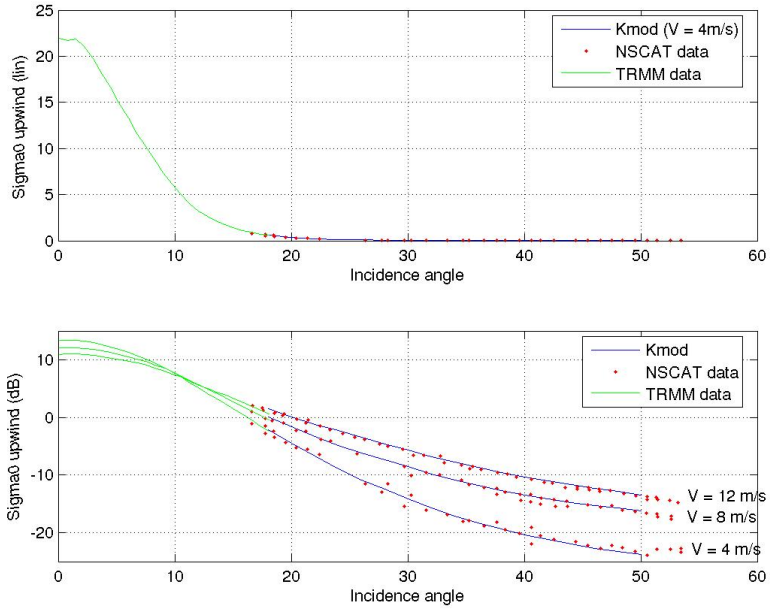

Figure 2: top: linear values of upwind Ku_band NRCS for TRMM data (green curve), NSCAT data (red points) and Kmod model function (blue curve), for V = 4 m/s. Bottom: values in dB of upwind Ku_band NRCS for TRMM data (green curve), NSCAT data (red points) and Kmod model function (blue curve), for V = 4 m/s, 8 m/s, and 12 m/s.

It shows that, at Wavemill incidence angle, the radar cross section increases by only 4dB with wind speed increasing from 4 m/s to 20 m/s, when it increases by 16 dB at 48 degrees of incidence angle.

This might be a problem for the current or past 3-antenna scatterometer systems. For example, NSCAT retrieved wind speed (Ebuchi, 2000) does not exhibit systematic dependency on the incidence angle but is very sensitive to the calibration of the geophysical model function at low incidence angles. Ebuchi showed that refining the NSCAT-1 calibration to improve the high wind speed retrieval had side effects and results in quite larger wind speed standard deviations for the NSCAT-2 model function at low incidence angle. If it might be a problem with the 3-antenna scatterometer systems, it could be a more severe one if the azimuthal diversity of a system such as Wavemill is not sufficient. On the other hand, a very high signal to noise ratio should be reached at km-scale for Wavemill to help satisfy wind vector accuracy specifications, supposing the wind direction dependency can be well resolved in any way (2 orthogonal antennas, Doppler measurements, …..). This will be investigated in the part dedicated to the error analysis and numerical simulations.

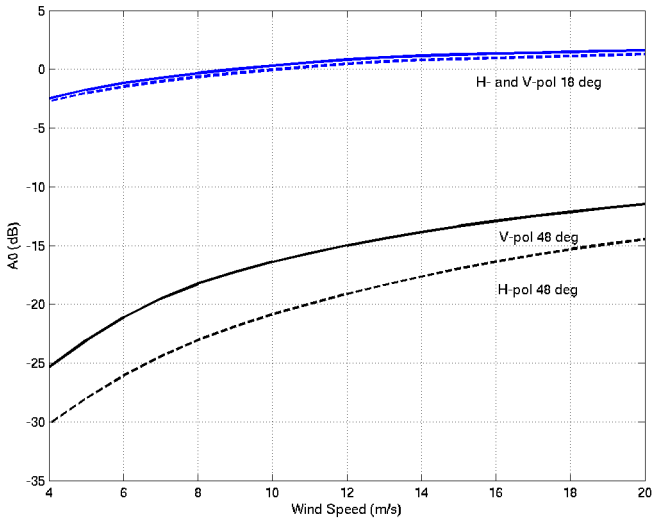

Figure 3: A_{0P} *(dB) predicted by the Kmod model as a function of wind speed at VV-pol (solid lines) and HH-pol (dashed line) for 18 degrees (blue lines) and 48 degrees (black lines) of incidence angle.*

If the NRCS sensitivity to wind speed is low at off-nadir low incidence angles, its azimuthal modulation is also very reduced. It is expressed with the A_{1P} and A_{2P} terms in equation (1). To illustrate this reduced sensitivity, the Figure 4 shows the Kmod *A2/A0* quantity, related to the upwind/crosswind ratio (the relative NRCS variation when viewing orthogonal wind directions), as a function of incidence angle at H- and V-pol. For incidence angles lower than 20^{o} the A2/A0 term is lower than 20%, which is quite low, and it increases quickly with incidence angles to reach 60% near 50^{o} of incidence angle.

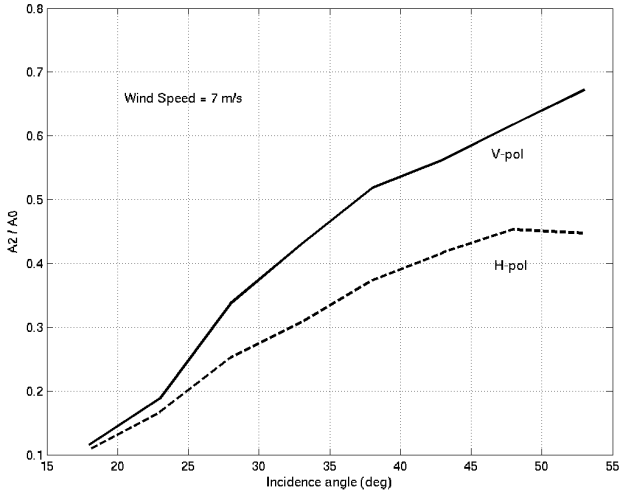

Figure 4: A2/ A0 computed from Kmod coefficients as a function of incidence angle at V-pol (solid line) and H-pol (dashed line).

This has important consequences when estimating the wind direction with scatterometer systems operating at low incidence angles. Figure 5 shows the dependence of wind direction distribution, in a frame related to the antennas system, of NSCAT retrieved winds and of colocated ECMWF winds on ground cell location. Cells 1–3 and 22–24 correspond to the cells of high incidence angles at the left and right swaths, respectively. It is shown that the directional distribution depends on incidence angle, which is not geophysically consistent. Moreover the NSCAT distributions show spikes not apparent in the ECMWF distributions and these spikes are more significant at inner cells, i.e., low incidence angles. Retrieved wind directions are trapped in particular azimuths relatively to the antennas system. This is the result of the low NRCS azimuthal sensitivity at low incidence angles and associated errors in the GMF calibration.

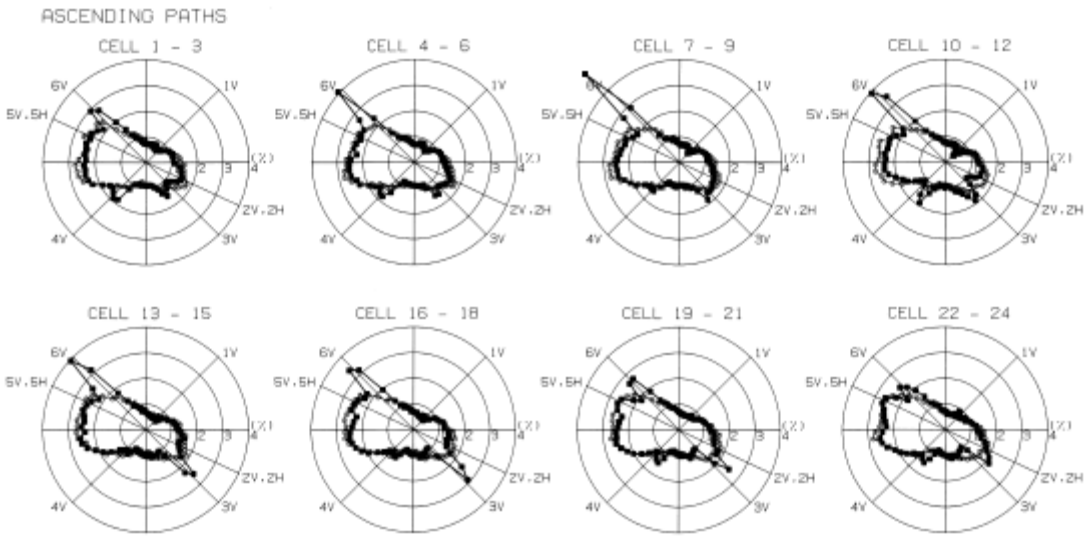

Figure 5: Wind direction distribution, in a frame related to the antennas system, of colocated NSCAT winds (black squares) and ECMWF winds (open circles), for different cell locations (incidence angles). After Ebuchi (2000).

Other considerations may impact the applicability of the Wavemill SAR operation to resolve wind direction.

Other consequence of low incidence angle is the impact of sea state maturity on the NRCS variability. This has already been investigated for C-band ERS observations (Quilfen et al., 2004). Furthermore for Ku-band systems, this can be analyzed and quantified at low incidence angle by using a large colocated data sets pairing TRMM NRCS and Jason-1 and Envisat altimeters. The Figure 6 displays a difference factor between averaged TRMM PR σ_0 associated to a 1-m class of significant wave height (SWH) and the averaged values estimated over all SWH, as a function of incidence angle and for various SWH classes at selected wind speed. For all winds, behavior of the difference factor as a function of SWH is clear. At low SWH representing young seas, the factor decreases with increasing angle, whereas for higher SWH associated with mixed seas including swell it exhibits the opposite trend. At incidence angle of 18^o, close to the Wavemill configuration, the difference factor between extreme seas conditions (1m to 6m SWH) is greater than 1 dB at 2 m/s and 5 m/s and greater than 0.5 dB at 7 m/s and 10 m/s.
This is a relatively large SWH impact on NRCS given the reduced sensitivity to wind speed at Wavemill incidence angles. But, it should be emphasized that such NRCS measurements, including effects of SWH or current, are closer to the desirable true wind forcing (i.e wind stress over the sea surface) than the GMF-retrieved wind vector. Although it is beyond the scope of this study to discuss retrieval of such quantity, it is relevant to the discussion in this study concerning retrieval of both surface wind vector and surface current from Wavemill measurements. We can here refer to a recent study by Plagge et al. (2012) who analyzed the surface current effects on both ASCAT and QuikScat retrieved wind vectors to show that the NRCS measurements are significantly impacted by surface current measurements and confirm former studies by Quilfen et al. (1999) and Kelly et al. (2001). The Figure 7 shows that the estimated QuikScat wind vectors are biased as a function of surface current whatever the resolution of the QuikScat wind cell.

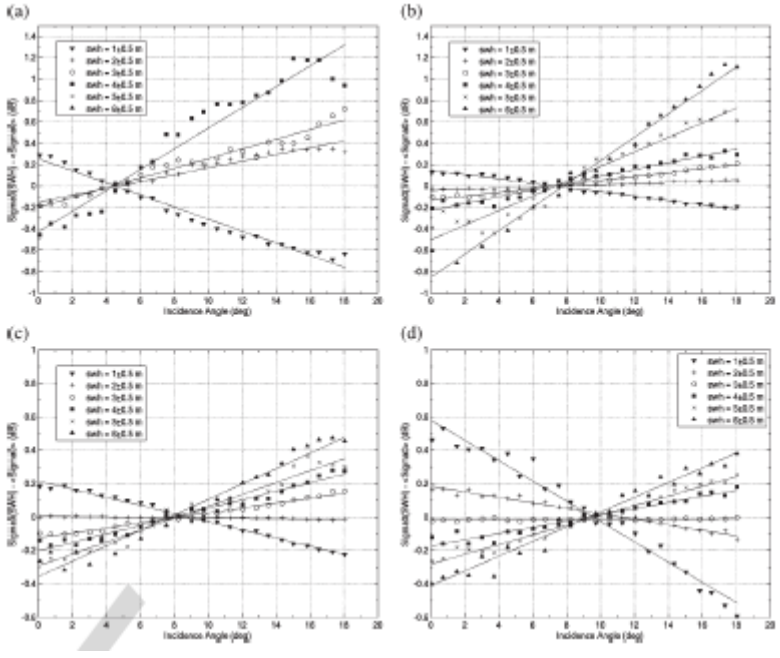

Figure 6: Difference factor between averaged PR σ_0 associated to a 1-m class of significant wave height (SWH) and the averaged values estimated over all SWH, as a function of incidence angle and for various SWH classes at selected wind speed: (a) 2 m/s, (b) 5 m/s, (c) 7 m/s, (d) 10 m/s.

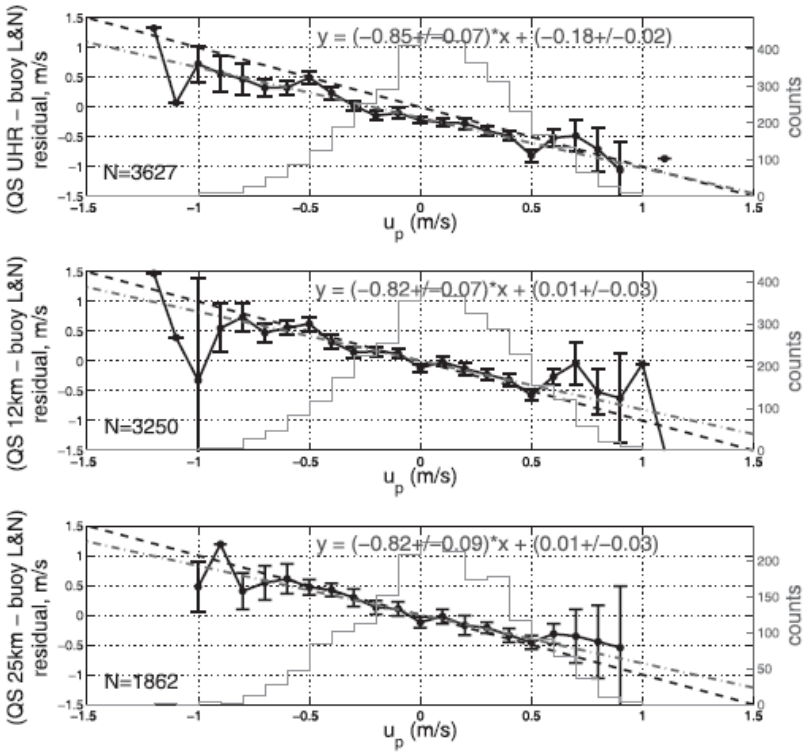

Figure 7: Bin-averaged wind speed differences (QuikSCAT - buoy) vs Up (10 cm s^{-1} bins). Error bars represent the standard error within each bin. The black dashed curve represents a -1:1 line while the gray dotted–dashed is the result from a weighted linear regression. The sample population is noted in each panel. From Plagge et al. (2004).

3.2 Inversion of the synthetic cross sections and Doppler anomalies to retrieve the wind vector and error analysis (WP3200)

3.2.1 Theoretical background

The potential to combine the mean Doppler information obtained under different azimuth with the RCS measurements is a very important feature of the Wavemill concept, and this shall be assessed.

To this end, model developments (e.g. Mouche et al., 2008) can be extensively used to study the combined RCS and Doppler wind direction sensitivity as function of incidence angle and wind speed.

To note, the possibility of retrieving wind speed information from the combined polarization information present in a SAR data product may also be worth considering. This has been anticipated within the Polarimetric Radiation Experiment led by ESA EOPP in 1996 (Chapron et al., 1997), and was illustrated using NSCAT data (Quilfen et al., 1999). Newly available RADARSAT-2 Quad-Pol data have also been recently used to demonstrate new analysis capabilities (Kudryatsev et al., 2013). Also anticipated, the Doppler anomalies are polarization dependent, HH measurements leading to larger Doppler than VV ones.

The new resource for SAR wind inversion can thus build on the available single or dual-polarization Doppler information. General approach shall follow developments presented in Chapron et al. (2005), and more recently described in Mouche et al. (2012) showing how the Doppler centroid anomaly could be used to retrieve geophysical information about both wind and sea surface current. As mentioned above, a residual Doppler comes from the line-of-sight motions of the surface scattering elements relative to the fixed Earth, as illustrated in Figure 8.

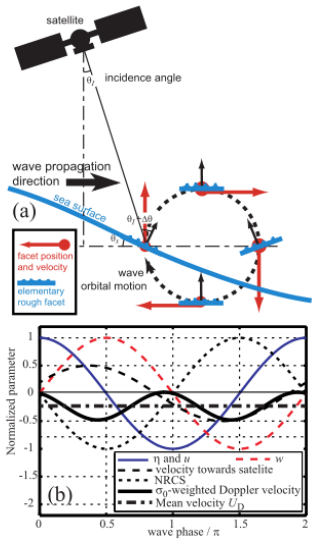

Figure 8: Schematic of the conceptual model of the measurement of surface velocity and the contribution of radar cross-section modulation by waves and (b) example of parameters over a sinusoidal wave (after Chapron et al., 2005).

Accordingly, in the absence of an underlying sea surface current, the Doppler shift induced by the near surface wind is interpreted as the mean line-of-sight velocity of the radar detected scatter elements. Independent of the local scattering mechanism (Bragg-like, specular, ...), the velocity of roughness elements is first fixed and related to their phase velocity. Yet, as tilted by longer waves, instantaneous Doppler and NRCS shall vary along these moving wave profiles, leading to correlation with horizontal and vertical orbital velocities. Consequently, the overall Doppler is shifted and is first strongly dependent upon the strength of the tilt modulation. Thus, for a given incidence angle and wind direction, the Doppler shift increases with increasing wind speed. For a given incidence angle and wind speed, the Doppler is also strongly dependent on the wind direction relative to the antenna look direction. The Doppler shift reaches a maximum (minimum) in upwind (downwind) configuration and becomes zero when the wind is blowing in the azimuth direction. The Doppler shift is thus sensitive to the wind direction, which is particularly interesting for SAR wind retrieval, as reliable wind direction estimates are rare. The figure 9 illustrates the modeled behavior of the Doppler shift at C and Ku bands (Mouche et al., 2008).

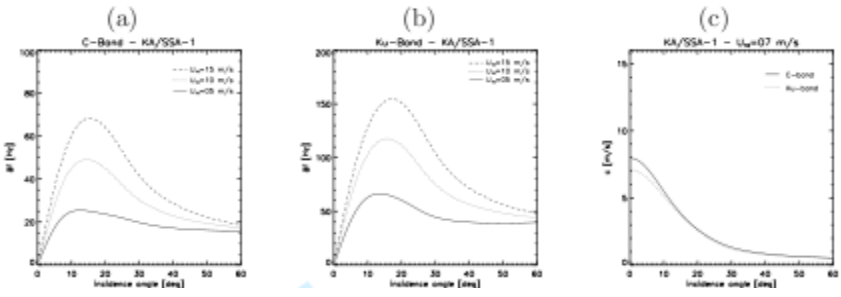

Figure 9: Doppler frequency at a) C-band and b) Ku-band predicted as a function of incidence angle in upwind configuration. c) Sea surface velocity projected along the line-of-sight of the radar.

The feasibility of this technique certainly needs to be further examined, especially in the context of the Wavemill instrument and particular configuration. It is to be noted that, today, Wavemill does not use polarimetry, but choices could be made between VV or HH configurations.

Results of the analysis should lead to conclusions about the necessary configuration to retrieve information about wind information and, more importantly, wind induced surface motion.

3.2.2 Data and tools

As already discussed in the 3.1 paragraph, we will mainly use, for the Ku-band NRCS data, the NSCAT and TRMM Precipitation Radar (PR) data and GMFs since the configuration of these missions matches the Wavemill configuration concerning the working frequency and the incidence angle of measurements. At C-band, we will use the Envisat SAR NRCS data and the CMOD5_N GMF NRCS data. VV and HH data are available.

For the Doppler shift data, Ku-band data are not available. We will then use data predicted using the RCA (Mouche et al., 2008), as illustrated in Figure 7, or DopRim (Hansen et al., 2012) theoretical models, and the C-band data used in the Envisat SAR processing (Chapron et al., 2004). We will more especially use the empirical model derived from these Envisat data, the so-called CDOP empirical GMF. VV and HH data are available.

Although the Wavemill operating frequency should be Ku-band, C-band data are used to try to infer Ku-band Doppler shift information from these data.

A coherent ensemble of Matlab codes has been set up that contains these empirical and semi empirical/physical backscattering and Doppler shift models.

It enables practical and fast comparison of these models as shown in Figure 10.

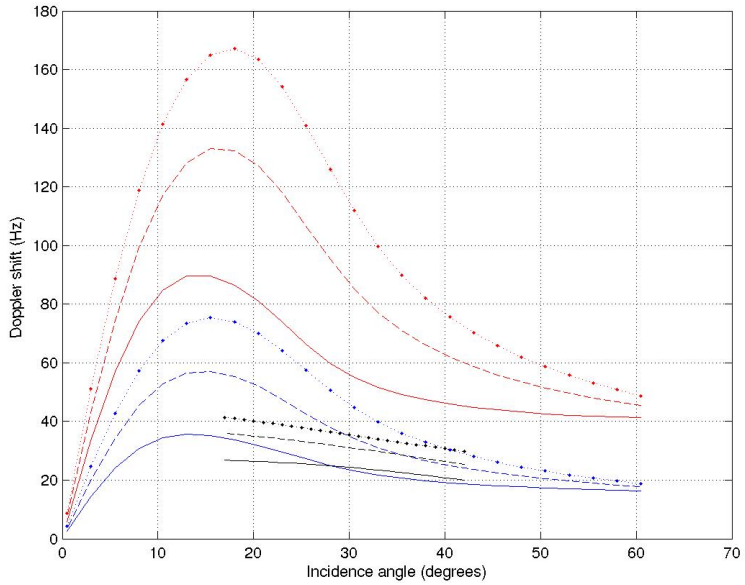

Figure 10: Doppler shift (Hz) data predicted by the RCA model at Ku-band (red curves) and C-band (blue curves) and predicted at C-band by the CDOP model (black curves), as a function of incidence angle and for 7 (solid lines), 12 (dashed lines), and 17 (dotted lines) m/s wind speed values.

3.2.3. Proposed Approach

The proposed approach will directly build on the methodology recently developed in Mouche et al. (2012). Using a Bayesian scheme, it has indeed been demonstrated how the two radar quantities, i.e., NRCS and Doppler anomaly, could be advantageously used to increase the performance of the SAR wind inversion schemes.

As demonstrated, single antenna SAR systems can provide mean Doppler and cross section information to better constrain wind vector retrieval algorithms. The wind inversion thus consists in a minimization problem of a cost function that was defined as follows for the Envisat SAR:

$$J(\vec{u}) = \underbrace{\left(\frac{\sigma_0 - KMOD(\vec{u})}{\Delta\sigma_0}\right)^2}_{a} + \underbrace{\left(\frac{df - KDOP(\vec{u})}{\Delta df}\right)^2}_{b} + \underbrace{\left(\frac{\vec{u} - \vec{u}_B}{\Delta\vec{u}}\right)^2}_{c}$$

3.2.3-a Definition of the function for the Ku-band Doppler shift

The Doppler shift f_D is related to the velocity, U_D , of a simple target of fixed shape moving along the surface by the following relationship:

$$U_D = -f_D / k_e \sin\theta$$

where k_e is the electromagnetic wave number and θ the angle of incidence of the radar beam relative to the normal to the surface. U_D is defined positive when the target moves away from the radar.

As shown in Chapron et al. (2005) for Envisat C-band data, the velocity can be related mainly to the wind speed, through the contribution of the short wind waves, and to a gain factor G accounting mainly for the tilt bias induced by larger waves. The following empirical relationship was then derived:

$$U_D = 0.022G\left[1. - 0.52\tanh\frac{U_{10||}}{25}\right]U_{10||} \quad \text{where} \quad G = (1/\sigma_0)(\partial\sigma_0/\partial\theta)$$

for $U_{10||} > 0$ and a slightly different empirical expression for $U_{10||} < 0$

This tilt bias accounts for more than 60% of U_D at incidence angles close to the Wavemill ones and reflects the correlations between local vertical velocities and surface slopes.

Combining the above equations we obtain a relationship linking the Doppler shift to the wind speed, the incidence angle, the gain factor, and the electromagnetic wave number.

$f_D = Ck_e \sin\theta G f(U_{10||})$ where C is a constant

This relation can be illustrated / validated for Ku-band by comparing the behavior of available Ku-band measurements over the whole range of incidence (nadir to ~ 55°) to the behavior of the Doppler shift as predicted by the RCA model. The figure 2 in the precedent chapter presented the available data obtained from TRMM and NSCAT missions to show the general behavior of Ku-band NRCS and the coherency over the nadir to off-nadir incidence angle range.

The figure 11 gives, for different wind speed values, the behavior of the term $\sin\theta * G$ computed using the above data, and that of the Doppler shift predicted by the RCA physical model. The right and left y-axis scales are changing to preserve the data dynamic range and to match the right and left axes curves. As predicted by the equation $f_D = Ck_e \sin\theta G f\left(U_{10||}\right)$, at fixed wind speed, both quantities increase quickly from 0 at nadir to a maximum at ~ 15 degrees of incidence angle, then decrease slowly to reach asymptotically a value mainly determined by the hydrodynamic modulations of short waves. The maximum value is determined by the tilt modulation where the waves are the longer and the faster. While the gain factor is decreasing with wind speed, the Doppler shift is increasing to map the contribution of the hydrodynamic modulation by short waves implicitly contained in the right-hand term of the above relation. These results give confidence in the above relation regarding to the general behavior but do not tell much about values of the predicted (RCA or empirical) values of Doppler shift. Indeed, differences are highlighted in Figure 11. Agreement is not as good at low wind speed and high incidence angle. Moreover, although the fit between TRMM and RCA curves is quite good, the NSCAT data show less dynamic range for the wind speed dependency of the maximum (whose location is close to the Wavemill incidence angle). It is now useful to relate these results to what can be infer from the existing Doppler measurements, at C-band, with the so-called CDOP empirical model which can then be taken as reference.

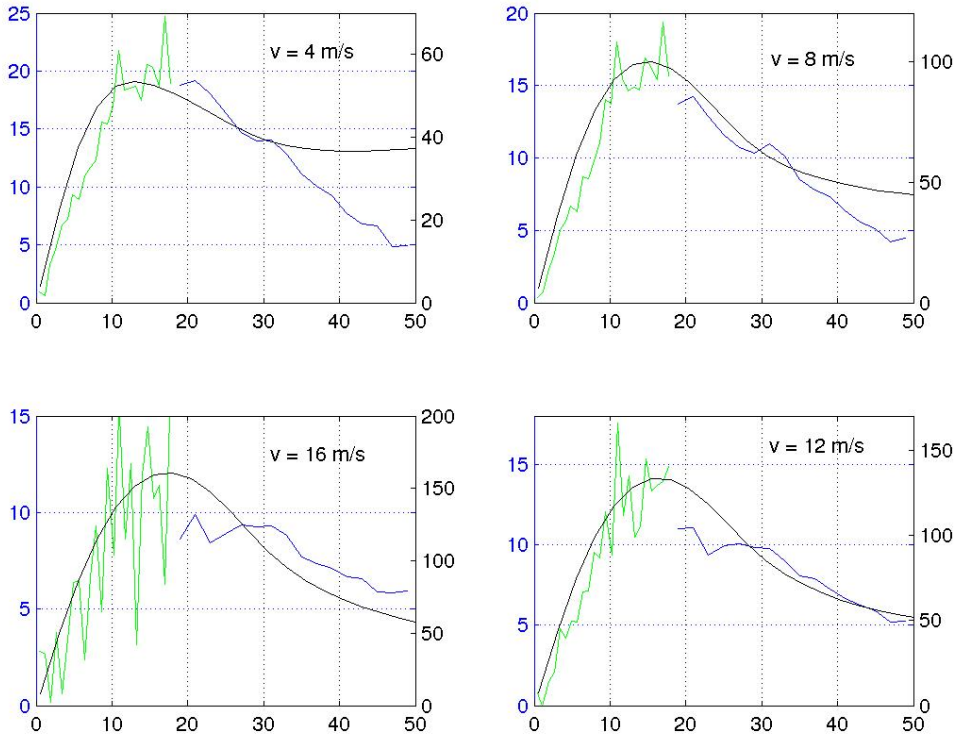

Figure 11: Left axis: Gain factors computed using Kmod (blue curve) and TRMM σ_0 data (green curve), as a function of incidence angles and for different wind speed. Right axes: Doppler shift (Hz) predicted by the RCA model (black curve), as a function of incidence angles and for different wind speed.

The figure 12 presents at C-band, for a given wind speed and as a function of incidence angle, the factor $\sin\theta * G$ (left axis) computed using CMOD5 and Envisat data for the σ_0 values, together with the predicted RCA and CDOP Doppler shifts (right axis). The y-axis right scale is changing as a function of wind speed to preserve the large dynamic range of RCA values.

The gain factor $\sin\theta * G$ computed using either CMOD5 predicted σ_0 or Envisat σ_0 data are as expected in good agreement. It decreases as a function of incidence angle and as a function of wind speed. The decrease rate as a function of incidence angle is in remarkable agreement with CDOP, to give confidence in the above heuristic reasoning. The RCA Doppler shift values exhibit much faster decrease as a function of incidence angle. Moreover, RCA maximum values near the Wavemill incidence angle range are much larger than the CDOP ones, except at the lowest wind speed. Such differences between RCA and the Doppler data make the RCA Doppler shifts hardly usable for the Wavemill wind inversion cost function.

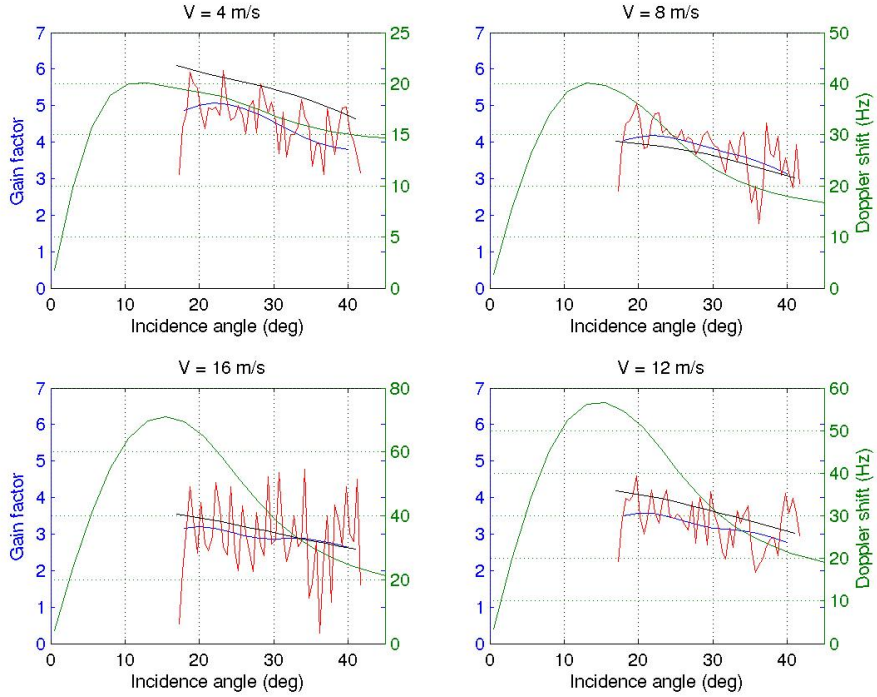

Figure 12: Left axes: Gain factors computed using CMOD5 (blue curve) and Envisat σ_0 data (red curve), as a function of incidence angles and for different wind speed. Right axes: Doppler shift (Hz) predicted by the RCA model (green curve) and by the CDOP model (black curve), as a function of incidence angles and for different wind speed.

The figure 13 presents at C-band and Ku-band, for a given wind speed and as a function of incidence angle, the factor $\sin\theta * G$ computed using CMOD5 and KMOD for the σ_0 values, respectively. We again find consistency with RCA for the general behavior, i.e maximum Doppler shift values at slightly larger incidence angle for Ku-band, and the maximum being shifted towards larger incidence angles with increasing wind speed. Mean values are comparable at C- and Ku-band but with significant differences depending on the incidence angle range. Near the Wavemill incidence angle range, while the gain factor is flat at C-band, it changes significantly at Ku-band between 18° and 23° of incidence angle. At 23°, the gain factors are comparable at C- and Ku-band while they are much more different at 18°. It is thus difficult to give a practical rule to infer meaningful Ku-band Doppler shift data from these data.

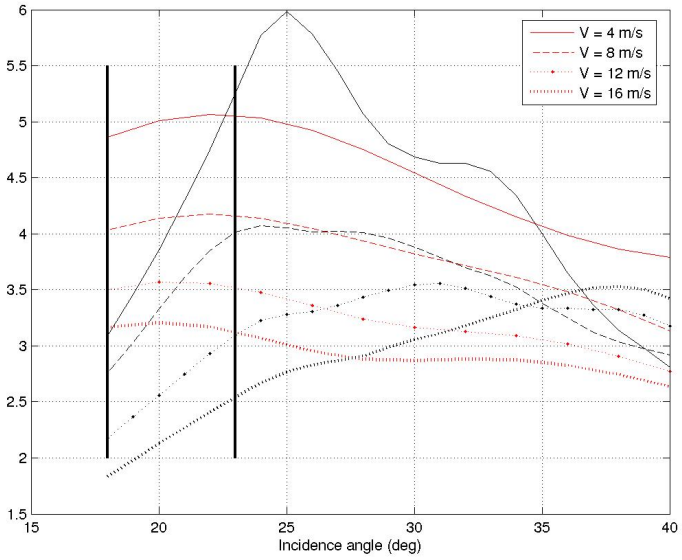

Figure 13: Gain factors $\sin\theta * G$ *computed at C-band using CMOD5 (red curves) and at Ku-band using a model fitted to* σ_0 *data (black curves), as a function of incidence angles and for different wind speed. The two vertical black lines give the Wavemill incidence angles.*

In the frame of this study, we can envisage a very simple and practical approach to derive a Ku-band model from the C-band one, accounting for: 1) the fact we only need rough estimates of Ku-band Doppler shifts to perform numerical simulations; 2) the fact that the very limited range of Wavemill incidence angles makes things easier.

The Figure 14 shows that the sea surface velocity U_D, as predicted by RCA, is very close at C- and Ku-band in the Wavemill incidence angle range. Following the relationship $U_D = -f_D / k_e \sin\theta$, we can infer the Ku-band Doppler shift f_D from the CDOP empirical data multiplied by a factor equal to the Ku/C wavenumber ratio. The results presented and discussed above could be used to enter in the error analysis that will be performed in the frame of the wind inversion numerical simulations.

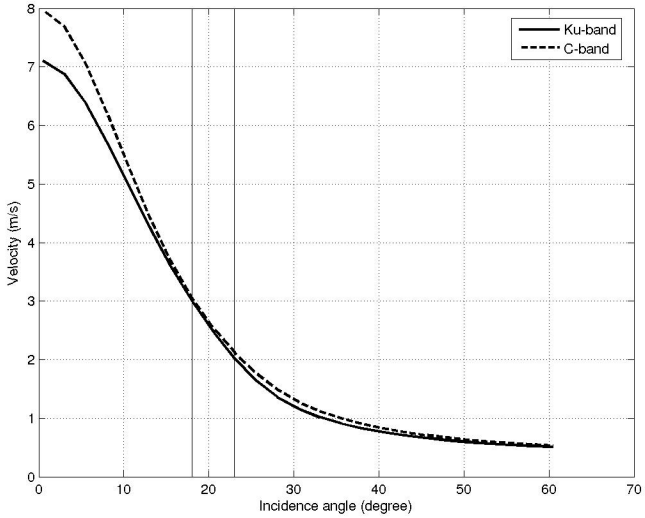

Figure 14: RCA predicted sea surface velocity in upwind configuration for 7 m/s wind speed.

3.2.3-b Influence of the antenna geometry on the cost function

Wind vector retrieval requires that the sea surface is observed under a variety of azimuths to maximize the expected upwind/crosswind modulation of the wind waves. The geometry and adequacy of past and current scatterometer systems have been reviewed in Portabella (2002). In the case of the two-antenna Wavemill geometry, the Ku-band predicted NRCS and Doppler shift data are plotted in Figure 15 to illustrate the gain obtained with the Doppler measurements. The wind speed is 7 m/s, the incidence angle 20° and the two antenna look at the sea surface with orthogonal azimuth angles. Arrows locate, for the example of 30° in wind direction, the 4 different solutions where the NRCS of both antenna are equal. Processing of a two-antenna system solely measuring the NRCS can only give four equally probable wind vectors. If the Doppler shift data is available, taking only the sign of this quantity for the two antenna enables to remove the ambiguity. This can be further illustrated by analyzing the behavior of different cost functions minimizing in a least-square approach the differences between the measured and modeled quantities.

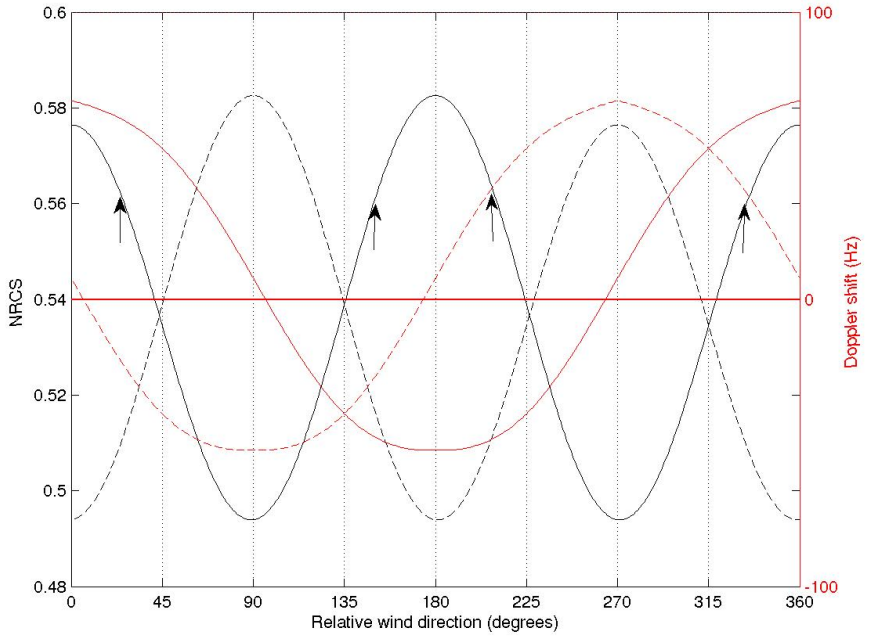

Figure 15: Normalized Radar Cross Section (left scale, black curves, NRCS in natural units) and Doppler shift (right scale, red curves, in Hz) as a function of the relative wind direction. 0 degree is upwind for antenna 1 (solid line) and crosswind for antenna 2 (dashed line). Arrows locate, for a given wind direction of 30°, the 4 different solutions where the NRCS of both antenna are equal.

The cost function for wind processing in the Wavemill configuration can be defined as follows:

$$J(\vec{u}) = \sum_{i=1,2} \left(\frac{\sigma_0 - KMOD(\vec{u})}{\Delta\sigma_0} \right)^2 + \sum_{i=1,2} \left(\frac{df - KDOP(\vec{u})}{\Delta df} \right)^2$$

By comparison with the Envisat case presented in Mouche et al. (2012) the function can include as many antennas as wished, i antenna index. The term controlling the proximity to an “a priori” (ancillary source) wind field is not present at this stage, precisely to analyze if the ambiguity removal can be performed by using solely the Wavemill measurements. The cost function is computed for a given “true” wind vector (Ut,Vt) and for the Wavemill geometry in the (U,V) wind components space. The minima of the cost function found for a given geometry correspond to the possible (the most probable in a bayesian scheme) wind vector solutions and their number depends on the geometry as already discussed. In this section, we present a graphical representation of the cost function for the different geometries and for a perfectly known wind vector, to discuss the weakness / strength of each configuration and to envisage choices for further steps. In the next section a simulation of the bayesian wind inversion will be performed using a Monte Carlo approach to characterize the expected errors for the various configurations and noise figures.

The figure 16 represents the cost function for a value of (7,0) m/s for the wind components (white cross) and (22,45) degrees for the incidence and squint angles which corresponds to a location somewhere inside the Wavemill swath. The looking azimuth is drawn as a white bar with the looking point at (0,0) and the white patch is the area where the wind speed is lower than 3 m/s and the cost function not computed. The top right panel corresponds to the 2-antenna geometry giving four equally-probable solutions if the NRCS only are used, as already illustrated in Figure 15. The top left panel corresponds to the Envisat one-antenna geometry and shows that two solutions are possible when only one NRCS and one Doppler shift are available. It is clear that in these two cases , shown in top panels, an a priori information is needed to remove the ambiguity which is mainly directional. The bottom left panel using only two Doppler shift measurements shows that a bayesian scheme would give one unique and well determined solution, giving the assumptions that the noise figures are adequate. This illustrates the potential of Doppler measurements to isolate the true wind direction. The bottom right panel shows the full configuration if all NRCS and Doppler measurements are used for a two-antennas Wavemill geometry. Retrieval is still improved for the wind speed estimation since the cost function presents a better defined shape close to the minimum. It means that a bayesian scheme processing real noisy values would give wind vector estimates closer to the “truth”. This is all the more important if we are interested in the residual surface current information. Aside this aspect that we will discuss further below , it can already be concluded that the Wavemill geometry at 22^{o} degree of incidence angle, and the foreseen low signal to noise ratio, can be fully exploited to provide high quality wind vectors at km-scale.

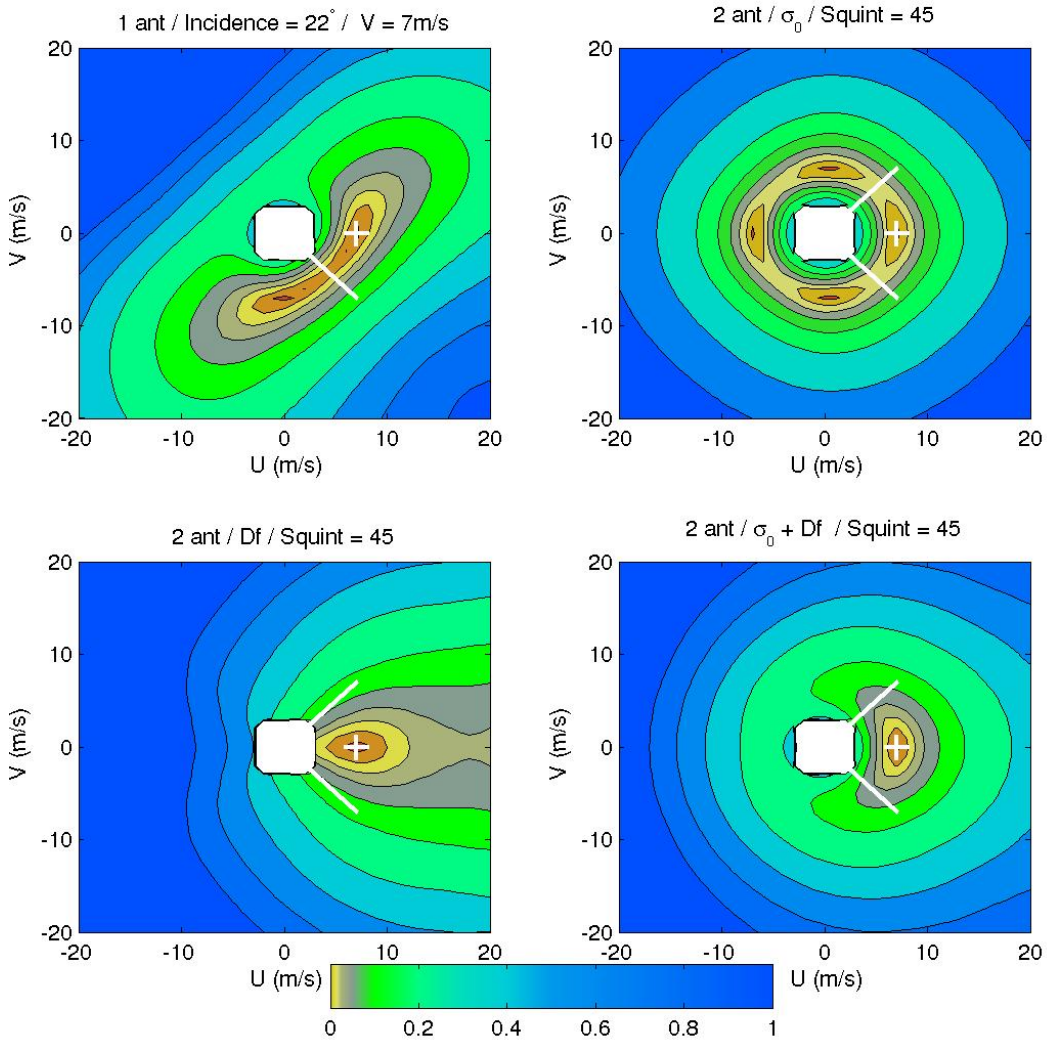

Figure 16: Cost function for a value of (7,0) m/s for the wind components (white cross) and (22,45) degrees for the incidence and squint angles. Top right: 2 antennas with NRCS only used; Top left: 1 antenna with NRCS and Doppler used; Bottom left: 2 antennas with Doppler only used; Bottom right: 2 antennas and NRCS and Doppler used. The looking azimuth is drawn as a white bar with the looking point at (0,0). The white patch is the area where the wind speed is lower than 3 m/s and the cost function not computed.

It is also interesting, for the discussion and for comparison with the standard ASCAT geometry, to show what would give a three-antennas geometry using only NRCS measurements. It is displayed in Figure 17, top panel. As shown the three-antennas configuration applied as for a standard scatterometer (no Doppler available) reduces the number of ambiguities to only two possible wind vectors separated by 180° in direction. Compared to the Wavemill configuration, bottom right panel, and beyond the fact that it leaves a 180° ambiguity in direction, its annulus shape makes it more sensitive to directional errors for noisy NRCS measurements, as further discussed in next section. However this 3-antennas configuration is interesting because the NRCS measurements are expected to be less affected by the surface currents, even if also significantly impacted (Plagge et al., 2012), than the Doppler measurements. In the presence of currents, wind retrieval using only the NRCS measurements (in an ASCAT configuration) may be informative (with additional rules to remove the directional ambiguity). This will be discussed in the last part of this workpackage. We then restrict to these two possible configurations, an ASCAT-like and a 2-antenna or 3-antenna Wavemill one , to analyze the effect of varying the squint angle on the results presented in Figure 16 and 17.

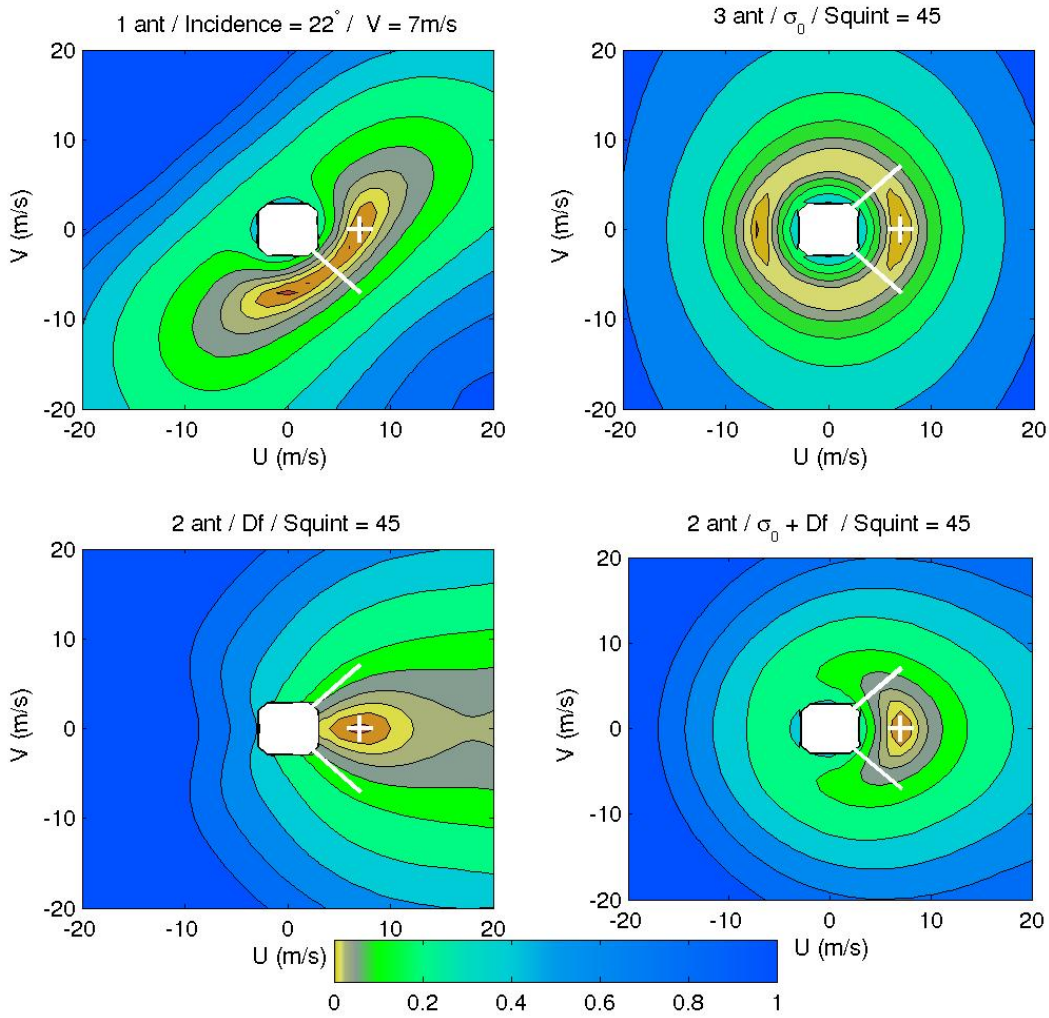

Figure 17: same as Figure 16, except the top right panel which presents a 3-antennas configuration.

Results are shown in Figure 18 for squint angles of 40° and 64° which correspond to the outer and inner part of the Wavemill swath, respectively.

As expected a configuration with a squint angle of 40° does not change much the results and the cost function local minima are located very close to the true wind vector. At 64° of squint angle, which corresponds to a separation of 128° in azimuth between the two lateral antennas, we again obtain the minimum of the cost function at the true wind vector location. It means that, for noiseless measurements, the azimuthal diversity, for the different configurations, is sufficient and will not introduce artifacts in the bayesian inversion process. It is however necessary to study this behavior for more realistic cases corresponding to noisy measurements and for a range of different wind conditions.

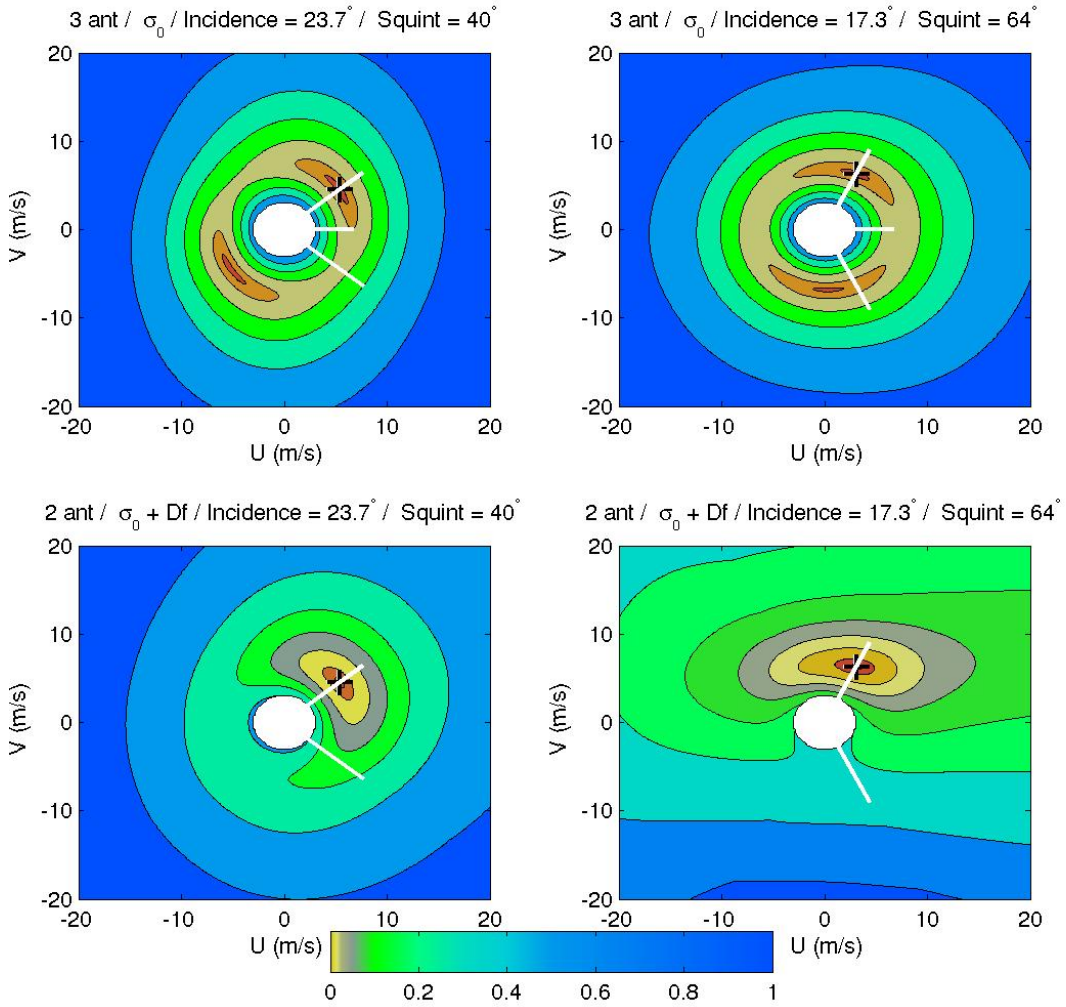

Figure 18: Top (Bottom): Cost function for a value of (7,0) m/s for the wind components (white cross) and 40º (64º) degrees for squint angle, for a 3 antennas geometry with NRCS only used (right panels) and a 2 antennas geometry and NRCS and Doppler used (left panels). The looking azimuth is drawn as a white bar with the looking point at (0,0). The white patch is the area where the wind speed is lower than 3 m/s and the cost function not computed.

3.2.3-c Monte Carlo simulation of the wind inversion scheme and performances

The graphical representation of the cost function as presented above gives the illustration of how the directional ambiguity depends on the sensor characteristics and showed that the Doppler shift parameter provided by the Wavemill configuration enables to fix it without having to use an ancillary wind information. It is now useful to quantify what would be the retrieved wind vector accuracy for the different configurations and realistic figures of noise for the NRCS and Doppler shift measurements.

Methodology

The behavior of the retrieved wind vector accuracy, in term of bias and root mean square error, has been statistically derived using a Monte Carlo approach. For a given wind vector, a “true” NRCS and Doppler shift (Df) have been computed from the GMFs (KMOD and KDOP) and a set of 1000 random NRCS and Df values have then been generated (using the normrnd Matlab function). The mean of the NRCS and Df normal distribution is equal to the true value and two different figures

have been defined for the normal distribution standard deviations. One is (5%, 5 Hz) and the other (3%, 3 Hz) for NRCS and Df respectively. Errors in NRCS and Df are uncorrelated and we then used 1000 (NRCS, Df) random pairs to process 1000 times the bayesian inversion scheme for each instrumental configuration (3 or 2 antennas, ASCAT-like or Wavemill ….). The inversion consists in finding the minimum of the cost function corresponding to one instrumental configuration. Given that we know the "true" wind vector, the minimum search is simplified by considering the search in an angular sector of +/- 60° around the true wind direction. With the chosen noise figures, the simulated data are indeed restricted within this sector where we obtain only one minimum of the cost function, whatever its definition (ASCAT or Wavemill configuration). From these 1000 realizations of the wind inversion, providing 1000 estimates of the retrieved wind vector for a given true wind vector, the mean bias and root mean square error are estimated. The choice for the noise figures are to be discussed, especially concerning Df for which little is known, but a strong hypothesis in this calculation is also that the GMFs are supposed to be error-free. This is not the case and different sources of error can be expected. We do not consider GMFs calibration errors, not because it is negligible but because it is not the scope of the study, but we will rather consider, farther in the workpackage, the errors associated with the GMFs definition, especially the effect of surface currents on the NRCS and Df measurements.

Results

The figure 19 shows the results, for a wind speed of 8 m/s and 45° of squint angle, as a function of the wind direction varying from upwind / fore antenna to downwind / fore antenna. The most prominent feature is that for the ASCAT configuration the bias and root mean square error (rmse) are wind azimuth dependent. This was already analyzed and discussed (Lin et al., 2012; Portabella, 2002) and is linked to the antennas system geometry and NRCS non linear behavior. The retrieved wind vector is trapped in particular direction relatively to the antennas system. This may be still amplified in case of GMF calibration errors which is expected especially at low incidence angles for which the upwind / crosswind modulation is low. The amplitude of these bias and rmse modulations depends strongly upon the NRCS noise values, the maximum of bias in wind direction decreasing from 6° to 2° when the NRCS noise is decreased from 5% to 3%, the later value being close to the ASCAT radiometric resolution. Stoffelen and Portabella (2006) showed that this problem was also depending upon choices in the cost function normalization and beam weighting, but neither of them was able to fix it definitively. As shown in Figure 19, this processing artifact is corrected when the Doppler information is introduced in the inversion. This is the result of the smooth, almost linear, and strong Df azimuthal variability which implies a more regular behavior of the cost function around the true minimum as illustrated Figures 16/18.
For a noise figure of (3%, 3 Hz) the wind direction rmse are close to 6° which is well beyond the required specifications. The wind speed rmse is larger for a Wavemill-like configuration as a result of less defined wind speed sensitivity and constraints and it will certainly require more tests concerning weighting of the different cost function terms to choose the better trade-off. Overall the results presented in Figure 19 assess that the foreseen Wavemill 2-antennas configuration is, as expected, an improvement over a classical ASCAT configuration since it solves the 180° directional ambiguity but also because it regularizes the behavior of wind retrieval errors. Adding a third antenna in a Wavemill configuration results only in slight improvement (green curves). These results have been obtained for a squint angle of 45°. The figure 20 presents the same calculations for squint angles corresponding to the outer and inner edges of the Wavemill 100km wide swath, i.e 40° and 64°, respectively.

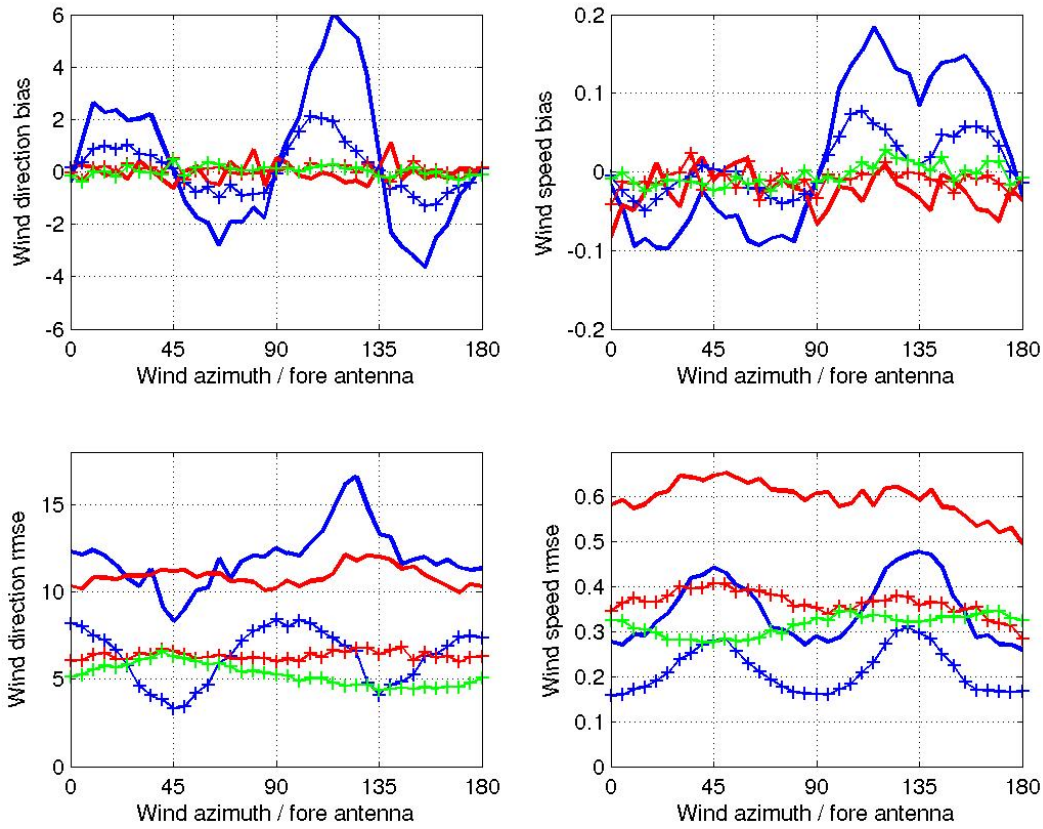

Figure 19: Wind speed (m/s, right panels) and direction (°, left panels) biases (top panels) and root mean square errors (rmse, bottom panels) as a function of the wind azimuth (°, 0 (180) corresponds to upwind (downwind) / the fore antenna) for a squint angle of 45° . The geometry configuration is for Wavemill 2-antenna (red lines) and 3-antenna (green lines), and ASCAT-like (blue lines) configurations and the noise figures are (5%, 5 Hz, solid lines) and (3%, 3 Hz, plus symbols) for the NRCS and Doppler shift, respectively. The wind speed has been set at 8 m/s.

The results for 40° of squint angle (Figure 20, solid curves) are, as expected, very close to those for 45°, although slightly degraded for the ASCAT configuration (blue curves). We obtain more significant differences at 64° of squint angle. Quite surprisingly, for the ASCAT-like configuration, the directions of the retrieved wind vectors are less affected by the trapping relatively to the antennas frame when the lateral antennas are not orthogonal. This can be easily explained by a simple drawing of antennas directional NRCS interdependency, as shown in Figure 21. At 45° of squint angle (left panel, red curve) the curve presents a sharp peak when the wind is upwind (or downwind) for one lateral antenna and crosswind for the other lateral antenna. For a true wind vector lying close to these particular azimuths on the curve, the effect of adding noise to simulate realistic measurements and then processing the inversion minimum search, will be to retrieve wind vectors lying exactly at these azimuths for most of the noisy measurements lying in the sector the farther to the curve. We thus obtain wind directions statistically biased towards these particular azimuths. At 64° of squint angle (same panel, blue curve), the non orthogonality makes the NRCS interdependency much smoother and it can be easily deduced that such “peak effect” almost does not occur. Moreover, the wind direction rmse is lower and more regular when the antennas are not orthogonal for the ASCAT-like configuration. In that respect, orthogonality of lateral antennas for a classical scatterometer perhaps does not give the most efficient azimuthal distribution for NRCS measurements. However, adding Doppler information mitigates quite efficiently this behavior as shown in Figure 20.

Conversely, all statistics are a little better for 40º of squint angle in the case of the Wavemill two-antennas configuration, antennas orthogonality being more efficient and artifact-free for the use of Doppler information.

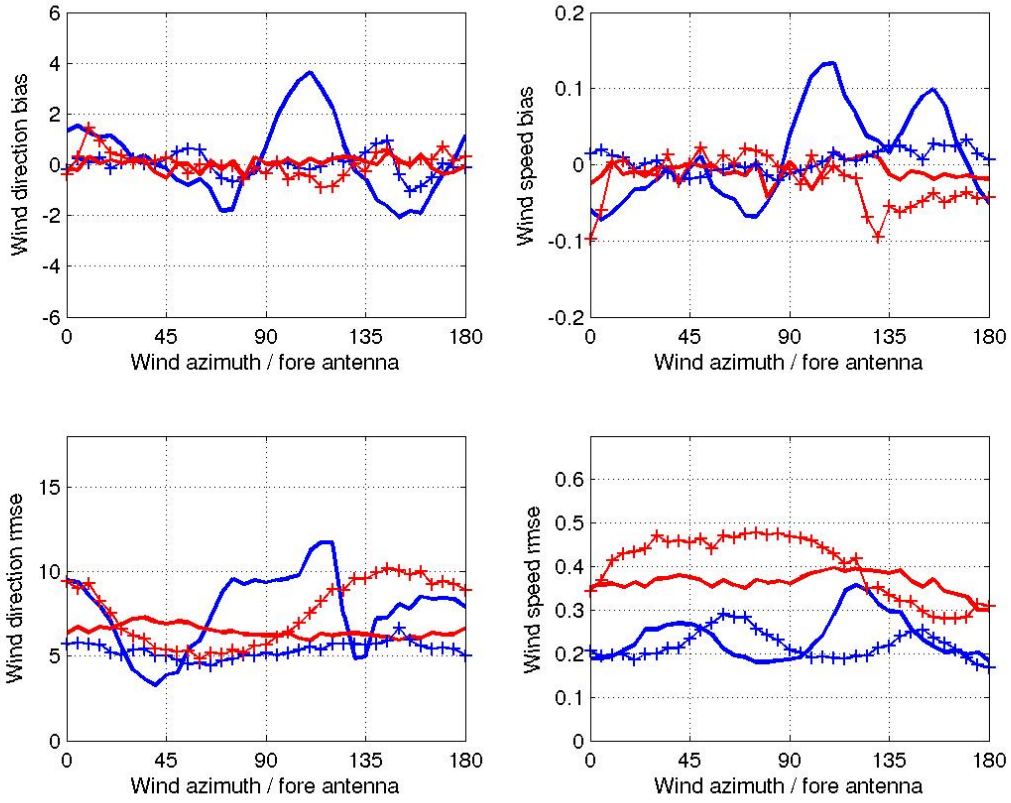

Figure 20: Wind speed (m/s, right panels) and direction (º, left panels) biases (top panels) and root mean square errors (rmse, bottom panels) as a function of the wind azimuth (º, 0 (180) corresponds to upwind (downwind) / the fore antenna) for a squint angle of 40º (solid lines) and 64º (plus symbols). The geometry configuration is for Wavemill 2-antenna (red lines) and ASCAT-like (blue lines) configurations. The noise figures are (3%, 3 Hz) for the NRCS and Doppler shift, respectively. The wind speed has been set at 8 m/s.

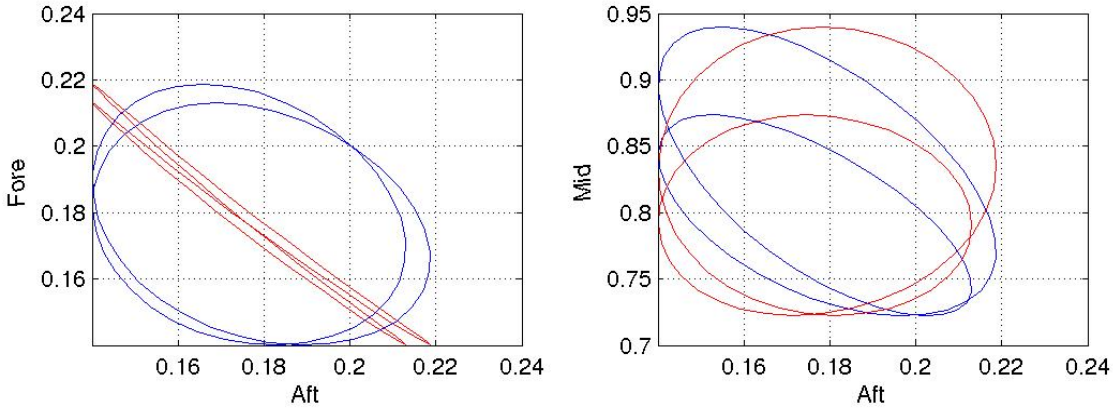

Figure 21: Variability of fore (left) and mid (right) antenna GMF-predicted NRCS as a function of aft antenna NRCS for a 360º range in wind direction and 8 m/s of wind speed. Red (blue) curves are for 45º (64º) of squint angle.

The above results have been obtained for a wind speed of 8 m/s which is close to the mean wind speed over the oceans. It is currently acknowledged that remote sensing of low wind speed conditions are more challenging because of a lower signal to noise ratio and a less defined sea surface geometry. In particular the NRCS azimuthal modulation (upwind/crosswind and upwind/downwind ratio) is significantly reduced. The figure 22 presents the results for a wind speed of 4 m/s (solid curves) and 8 m/s (dashed curves) for the ASCAT-like (blue curves) and Wavemill (red curves) geometry. The chosen noise figure is (3%, 3 Hz) for the NRCS and Doppler shift, respectively. Outputs of other workpackages should help to refine these noise figures. As shown, the bias and rmse behavior is comparable at 4 m/s and 8 m/s with directional errors larger at 4 m/s as a results of the lower azimuthal modulation predicted by the GMF. It is worth to remind that the NRCS and Doppler shift GMFs are supposed to be error-free in these Monte Carlo simulations which is not true in practice. Uncharacterized GMF errors are expected to be larger at low wind speed and low incidence angle.

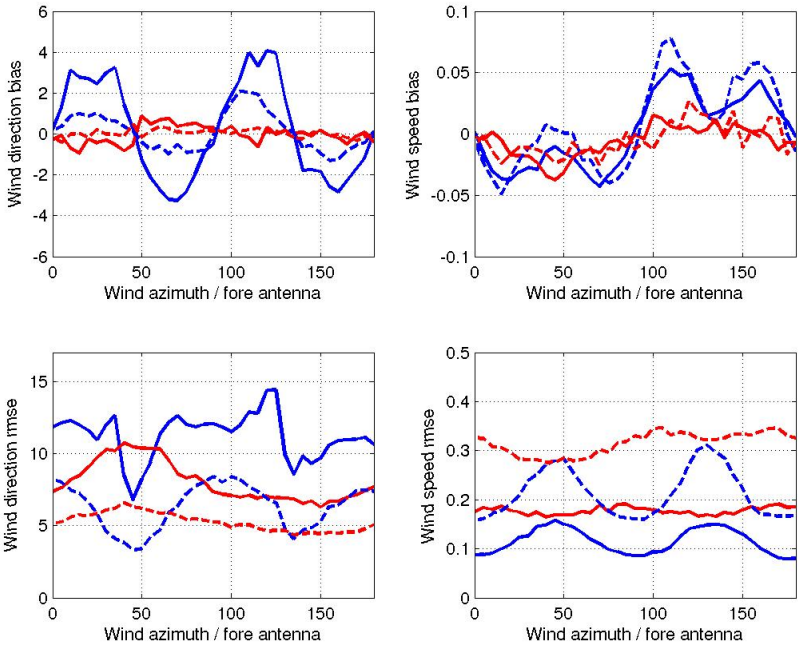

Figure 22: Wind speed (m/s, right panels) and direction (°, left panels) biases (top panels) and root mean square errors (rmse, bottom panels) as a function of the wind azimuth (°, 0 (180) corresponds to upwind (downwind) / the fore antenna) for a squint angle of 45° . The geometry configuration is for Wavemill 2-antenna (red lines) and ASCAT-like (blue lines) configurations and the noise figure is (3%, 3 Hz) for the NRCS and Doppler shift, respectively. The wind speed is 4 (solid lines) and 8 (dashed lines) m/s.

To conclude this investigation on the capability of the Wavemill concept to be used as a scatterometer, it can be assessed that the usual requirements in term of wind vector accuracy are fulfilled for the given Doppler shift and NRCS noise figures. However these noise figures, assumed to be achieved at km-scale resolution, may be refined depending on the Wavemill capabilities to satisfy technical requirements (WP4000 output). One obtained and expected result is that the Doppler shift information, provided by the Wavemill SAR-like processing, enables to solve the 180° ambiguity in the wind direction estimated from a standard bayesian wind inversion. This ambiguity is one of the most tricky problem with the standard scatterometry. It means that the use of an a priori wind information (ancillary information usually from a NWP numerical model) is not required, as for a standard scatterometer processing, for the two-antennas Wavemill concept. It has been also shown that the large Doppler shift sensitivity to the wind direction, at the quite low Wavemill incidence angles, help to regularize the wind vector errors as a function of the looking azimuth. Indeed, fixed fan-beam (ASCAT-like) and rotating fan-beam (CFOSAT-like) geometries

are shown to induce trapping of the retrieved wind directions in particular directions relatively to the antennas system when solely the signal intensity (NRCS) is used in the wind inversion (Lin et al., 2012).
Wind inversion results have also been presented in the case where a third antenna, looking in the across track direction, would be added to the current Wavemill concept. It has been done for two reasons: 1) it shows what would be gained from an ASCAT-like standard processing when the Doppler information is available; 2) it anticipates the Wavemill capability to be used as an ASCAT-like scatterometer if the Doppler information is not usable for any reason. Overall the third antenna NRCS and Doppler information help to gain only slightly in wind speed and direction accuracy, but would enable to perform an ASCAT-like standard processing as discussed in the next section. Finally, it appears that the across-track variability of the squint angle does not induce across-track change in the statistical distribution of wind vector errors, which is a good point.
As for the operational processing of past and current scatterometer data, it was assumed in these Monte Carlo simulations that the NRCS and Doppler shift information are uniquely related to the wind vector. This is explicit in the GMFs we have used but not true for real data. The effects of parameters such as the sea surface temperature, the atmospheric stability or the sea state are beyond the scope of this study. Here we then focus only on the effect of the surface current because retrieval of this Wavemill primary parameter can't be dissociated from wind vector retrieval, both being main contributors to Doppler data. As the WP3000 workpackage is dedicated to wind vector retrieval and not to surface current retrieval, we analyze in the next section the surface current effect in a sensitivity study of the wind inversion.

3.2.4 Sensitivity study

Surface currents contribute to the geometrical and kinematic properties of the sea surface and then modulate the NRCS and Doppler shift measurements. The impact of surface current on NRCS has been investigated using collocated buoy / scatterometer measurements (Quilfen et al., 2001; Plagge et al., 2012) to identify potential biases in the retrieved wind vectors. It has been established that the scatterometer winds represent winds relative to the moving sea surface but that only the satellite retrieved wind speed is current-relative, the wind direction being not significantly impacted. This has been quantified (Plagge et al., 2012) for ASCAT and QuikScat to give linear statistical models that correlate more or less with data depending on wind conditions and atmospheric stability. If the relationship between satellite winds and surface current has been well established and can be used to discuss order of magnitude of the induced satellite wind speed biases, theoretical developments relating the NRCS with the wind-wave field and surface current are not still usable in a wind inversion sensitivity study, i.e to inject a current-modified NRCS in the wind inversion process. We then assume that, at first order, the NRCS measurements are not affected by surface currents.
As a first increment of the wind/current retrieval problem, it is then straightforward to analyze the effect of a current-modified Doppler shift on the results obtained in the previous section. Indeed the Doppler shifts induced by a surface current of 1 m/s and a wind speed of 8 m/s are the same order of magnitude.
The sea surface velocity is now assumed to have both a wind-induced and a surface current-induced part, both contributing only for their in line of sight component. It can be written as follows:

$U_D = \gamma U_{10\|} + U_{c\|}$ where γ is found close to 0.2 for 23° of incidence angle and moderate wind conditions and a fully-developed sea.
The current-induced Doppler shift f_c is related to the velocity $U_{c\|}$ by the following relationship:

$$f_c = -U_{c\|} k_e \sin\theta$$

The figure 23 presents the cost function values of the bayesian scheme for a 8 m/s wind vector upwind for the fore antenna with an input Doppler shift modified to account for a 1 m/s surface current in the cross-track direction (thus with an angle of 45° with the wind vector). The upper left panel shows that the ASCAT-like configuration (no Doppler) is as expected not impacted. Results for other panels show that the retrieved wind direction is nearly aligned with the surface current and that the retrieved wind speed is, as expected, larger than the true one. The three-antennas configuration (bottom right panel) enables to reduce this wind speed bias. These results however depend on the weighting of the cost function terms, but show that, in presence of current, the Doppler information cannot be used in a blind way. Even weaker surface currents will affect too much the Doppler measurements, as indicated by the results presented in Figure 24 for a 0.5 m/s surface current and a varying angle between the wind and the surface current.

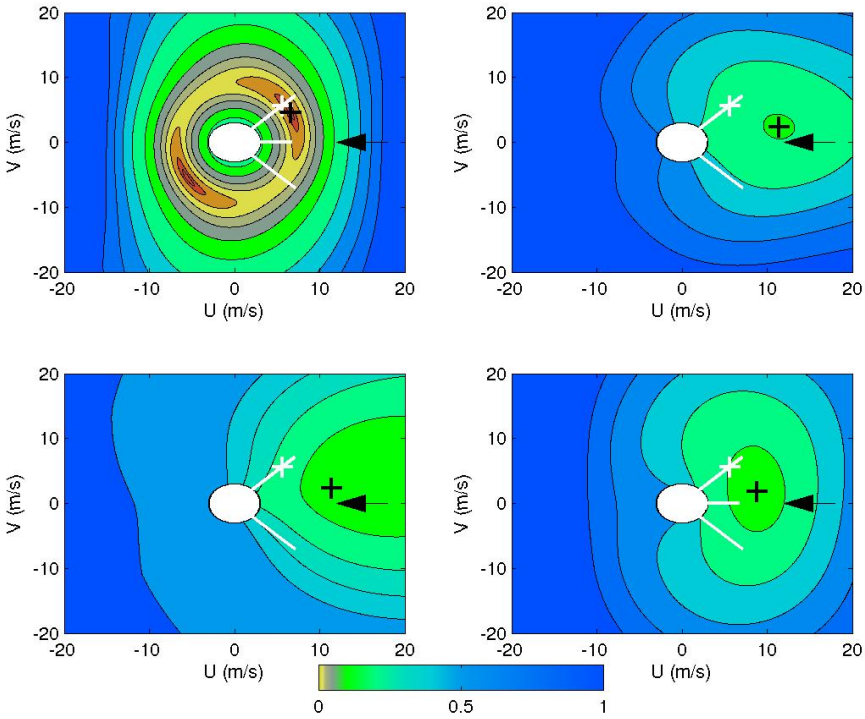

Figure 23: Cost function for a wind vector of 8 m/s upwind for the fore antenna (white cross) and (25,45) degrees for the incidence and squint angles. Top left: 3 antennas with NRCS only used; Top right: 2 antennas with NRCS and Doppler used; Bottom right: 3 antennas with NRCS and Doppler used; Bottom left: 2 antennas with Doppler only used. The looking azimuth is drawn as a white bar with the looking point at (0,0). The white patch is the area where the wind speed is lower than 3 m/s and the cost function not computed. The black cross locates the retrieved wind vector for each configuration and the black vector features a 1 m/s a cross-track surface current.

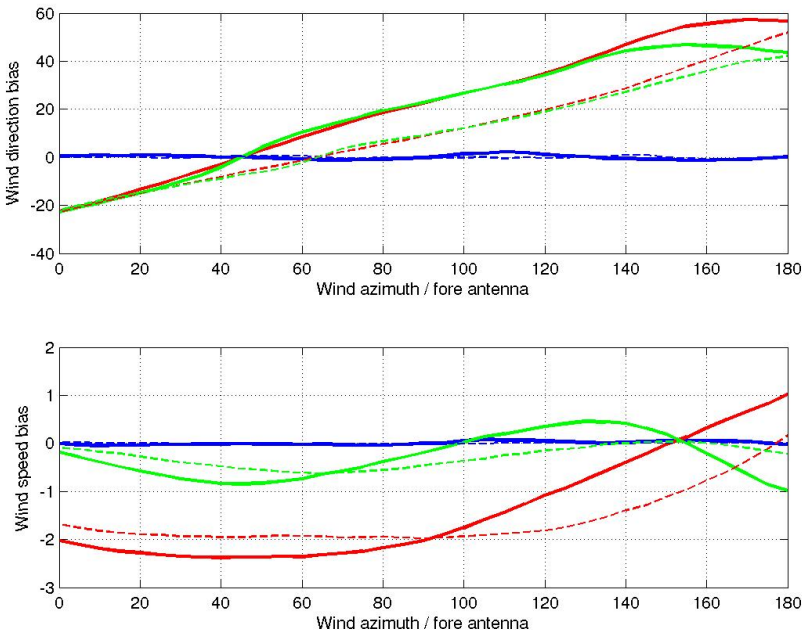

Figure 24: Wind speed (m/s, bottom panel) and direction (°, top panel) biases as a function of the wind azimuth (°, 0 (180) corresponds to upwind (downwind) / the fore antenna) for a squint angle of 45° (solid lines) and 64° (dashed lines). The geometry configuration is for Wavemill 2-antenna (red lines), Wavemill 3-antenna (green lines), ASCAT-like (blue lines) configurations and the noise figure is (3%, 3 Hz) for the NRCS and Doppler shift, respectively. The wind speed has been set at 8 m/s and the surface current at 0.5 m/s cross-track.

The top panel shows that even a quite low surface current induces unacceptable large wind direction errors (red and green curves) whatever the angle between the true wind and the current (except if they are aligned). There is almost no difference between a Wavemill 2-antennas or 3-antennas configuration. For the wind speed (bottom panel), a third antenna allows to better constrain the wind speed solutions, as already discussed in the previous section. The use of Doppler information for wind inversion thus requires either to verify in a first step that it does not contain a current signature before wind retrieval, either to envisage retrieval of both quantities in a dedicated wind/current inversion. In the frame of this workpackage, we concentrate on the first approach to find a way to flag the current-contaminated Doppler measurements.
A rule would be to verify that the local Doppler and cross-section measurements are consistent with the empirical models when applied to expected local wind conditions. The local wind conditions can be given by ancillary information (NWP model wind) or as a result of the Wavemill wind inversion. As one objective of the scatterometer wind processing is to rely as less as possible on ancillary information, we present in Figure 25 the residuals of the wind inversion, i.e the cumulative distribution function (cdf) of the NRCS residuals for different antenna geometries. The wind inversion cost function is defined as:

$$J(\vec{u}) = \sum_i \left(\frac{\sigma_0 - KMOD(\vec{u})}{\Delta\sigma_0} \right)^2 + \sum_j \left(\frac{df - KDOP(\vec{u})}{\Delta df} \right)^2$$

with i being equal to 3 to feature the standard ASCAT-like processing and j being equal to 2 or 3 to investigate the impact of a two- or three-antenna Wavemill geometry . The NRCS residual is then:

$$x = \sum_i \left(\frac{\sigma_0 - KMOD(\vec{u})}{\Delta\sigma_0} \right)^2$$

The hypothesis is that if the NRCS measurements are little impacted by surface currents but that Doppler shift measurements are more significantly impacted, the wind vector solution obtained from the NRCS + Doppler cost function minimization would be significantly different from the one that would be obtained from a standard (ASCAT-like) NRCS cost function minimization. It would then results in very different distribution for the NRCS residuals. The top panels in Figure 25 present the x cdf's in case of no current, for two angles between the surface wind and current (45° and 0°). In this no-current case, the ASCAT-like processing (blue curves) gives as expected the lowest values and adding two (red curves) or three (green curves) Doppler measurements in the processing results in slightly different wind solutions and then in slightly higher x values, in particular for the two-antennas configuration. However the distributions overlap to show that the NRCS, Doppler shift and retrieved wind vector data are consistent.
In case where a 0.5 m/s current is added in the Doppler data (bottom panels), the x cdf's for the cost functions containing the Doppler information give much higher x values and these distributions no longer overlap with the x distribution when solely the NRCS are used in the bayesian wind inversion. Although the x scale is too large in Figure 25, bottom panels, to separate visually well the blue and green curves, these two distributions are far to overlap. It should thus be efficient to define thresholds for the NRCS residuals in order to flag the data likely to be impacted by a surface current. For these data, the estimated winds should not be valid.

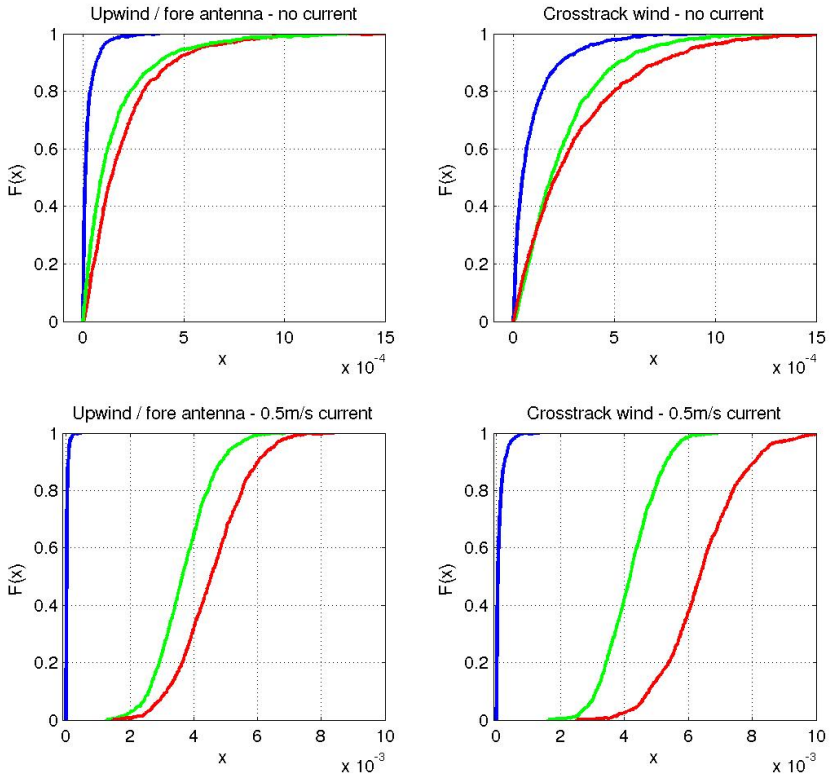

Figure 25: Cumulative distribution function of x values obtained from the 1000 iterations of the Monte-Carlo process for an ASCAT-like processing (solely NRCS, blue curve), a 2-(red curve) and 3-antenna (green curve) Wavemill processing (NRCS+Doppler), for a wind speed of 8 m/s and a wind direction upwind / fore antenna (left panels) and across-track (right panels). An across-track surface current of 0.5 m/s has been added for the results presented in bottom panels.

3.3 Discussion and recommendations

The Wavemill concept has been defined for surface current measurements as a result of previous studies analyzing the Doppler shifts related to the sea surface velocity. From these field experiments, high correlation are found between local cross section signals and Doppler signals. Translated to satellite observations, this correlation, mainly explained by the correlation between tilting and orbital motions, leads to overall detectable Doppler biases. Contrary to HF radar systems, satellite radar measurements cannot distinguish a precise Bragg scatter, and the overall Doppler bias is mostly driven by intermediate scale waves related to the tail of the wind wave spectrum and further depend upon the geometry of observations. Accordingly, direct surface current retrieval from Doppler analysis is, for most environmental conditions, not possible. Corrections must be performed to compensate the residual Doppler bias associated to detected wind induced surface motions. These corrections will, to first order be wind amplitude and direction dependent. Extracting the local wind speed and direction shall thus be essential to retrieve the residual Doppler associated to surface current.
This is the reason for which the Wavemill concept should also be defined as a wind instrument. Aside, and thanks to its SAR capability, it can be foreseen that Wavemill would have the potential to provide useful high resolution wind vector data to complement other sensors (scatterometer, SAR, radiometers).

A main goal for Wavemill definition works is thus to study the feasibility to retrieve estimates of the surface wind vector and their associated Doppler shift contributions from measurements of normalized radar cross section (NRCS) and total Doppler.

In the frame of this ESA WaPa project, and considering that the Doppler shift measurements are purely wind driven, it has been shown that the Doppler shift information provided by a two-antennas Wavemill SAR-like processing enables to solve the 180° ambiguity in the wind direction estimated from a standard bayesian wind inversion. This ambiguity is one of the most tricky problem with the standard scatterometry. It means that the use of an a priori wind information (ancillary information usually from a NWP numerical model) is not required, as for a standard scatterometer processing, for the two-antennas Wavemill concept. It was also shown that the across-track variability of the squint angles does not induce serious across-track change in the statistical distribution of wind vector errors. This study then demonstrates the capability of the 2-antennas Wavemill concept to be used as a scatterometer (usual requirements in term of wind vector accuracy fulfilled), for Doppler shift and NRCS noise figures at km scale better than 5 Hz and 5%, respectively. However as the definition of the noise injected in the Monte Carlo simulations does not include contribution of uncharacterized errors in GMFs or contribution of geophysical noise, the requirements for the instrumental noise should rather be better than 3 Hz and 3%.

In the case the Doppler shift contains mixed information from surface current and wind fields, it is concluded that the Doppler shift data cannot be used in the wind inversion scheme as defined. Using solely radar cross sections and ancillary wind information to help directional ambiguity removal is a possible way to estimate a wind vector independently of the Doppler measurements, but this is very sensitive to errors in the ancillary information (usually wind fields from a meteorological numerical model). Indeed, different wind vectors aliases are produced by such a two-antennas scheme and any shift in the ancillary wind spatial patterns, likely to occur frequently, will almost systematically result in the choice of a wrong alias. In favorable cases, the use of

directional wave information, extracted from the 50-meter pixel resolution images, could be used to help directional ambiguity removal. The quality of the ancillary wind information would also strongly benefit from the synchronization of the Wavemill orbit with another satellite carrying a scatterometer.

Alternatively to the foreseen two-antennas VV configuration, different solutions can be envisaged and are worth to be investigated in further study:

1) As shown, the add of a third antenna looking cross-track would be a reliable solution to mimic a standard ASCAT-like system using only radar cross-sections for the wind inversion. Specifications for this third antenna should not be as stringent as for the two antennas defined for the actual Wavemill system. This third antenna would not need to be operated in SAR mode and its operating frequency could be different than Ku to reduce its size.
2) Another interesting way still to be explored is to use VV and HH polarized measurements to filter for the surface current contribution in Doppler shift measurements. Indeed the surface current contribution to the Doppler shift is not polarization-dependent. As predicted from the CDOP and RCA models, the difference between VV and HH Doppler shifts is varying with wind speed and direction in an interesting way given the incidence angle is large enough. At 30^o of incidence angle and 5 m/s wind speed the Ku-band upwind/crosswind and upwind/downwind differences are close to 7.5 Hz and 15 Hz, respectively, while it is 1.5 and 3 Hz at 20^o of incidence angle.

More generally, to improve modulation of the radar cross section and of the Doppler shift measurements, it is recommended that Wavemill operates at higher incidence angles than those used for this study (18 to 25 degrees). Getting closer to 30^o would bring very significant benefit to extract a reliable wind vector from Wavemill measurements.

References

Bringer, A., C. A. Guerin, B. Chapron, A. A.Mouche, (2012), Peakedness Effects in Near-Nadir Radar Observations of the Sea Surface. *IEEE Transactions On Geoscience And Remote Sensing*, 50(9), 3293-3301. http://dx.doi.org/10.1109/TGRS.2012.2183605

Chapron, B., F. Collard, and F. Ardhuin, (2005), Direct measurements of ocean surface velocity from space: Interpretation and validation. *J. Geophys. Res*., vol. 110, p. C07008.

Ebuchi, N., (2000), Evaluation of NSCAT-2 wind vectors by using statistical distributions of wind speeds and directions. *Journal of oceanography* 56.2: 161-172.

Guerin C. A., S. Gabriel, B. Chapron, (2010), The weighted curvature approximation in scattering from sea surfaces. *Waves In Random And Complex Media*, 20(3), 364-384.

Hansen, M., V. Kudryavtsev, B. Chapron, J. Johannessen, et al. (2012), Simulation of radar backscatter and Doppler shifts of wave–current interaction in the presence of strong tidal current. *Remote Sensing of Environment*, 2012, 120(1): 113-122.

Johannessen J, B. Chapron, F. Collard, V. Kudryavtsev, A. A. Mouche, D. Akimov, K. Dagestad

(2008). Direct ocean surface velocity measurements from space: Improved quantitative interpretation of Envisat ASAR observations. *Geophysical Research Letters*, 35(22), 1-6

Kelly, K. A., S. Dickinson, M. J. McPhaden, and G. C. Johnson, (2001), Ocean currents evident in satellite wind data. *Geophys. Res. Lett.*, 28, 2469–2472.

Lin C.C., B. Rommen, J.J.W.Wilson, F. Impagnatiello, P.S.Park (2000), An Analysis of a rotating, range-gated, fanbeam spaceborne scatterometer concept. I*EEE Trans. Geosc. Rem. Sens.*, Vol.38, No.5.

Lin, C.C., M. Betto, M. Belmonte-Rivas, A. Stoffelen and J. de Kloe (2012), EPS-SG Windscatterometer Concept Tradeoffs and Wind Retrieval Performance Assessment. I*EEE Trans. Geosci. Remote Sens*., 50, 7, 2458-2472, doi:10.1109/TGRS.2011.2180393.

Mouche, A. A., Chapron, B., Reul, N., Hauser, D., & Quilfen, Y. (2007). Importance of the sea surface curvature to interpret the normalized radar cross section. *J. of Geophysis. Res*., 112(C10),DOI: 10.1029/2006JC004010 .

Mouche, A. A., B. Chapron, N. Reul, and F. Collard (2008), Predicted Doppler shifts induced by ocean surface displacements using asymptotic electromagnetic wave scattering theories. *Waves Random Complex Media*, vol. 18, no. 1, pp. 185–196.

Mouche A. A., F. Collard, B. Chapron, K.F. Dagestad, G. Guitton, J. A. Johannessen, V. Kerbaol, and M. Wergeland Hansen (2012), On the Use of Doppler Shift for Sea Surface Wind Retrieval From SAR. I*EEE Trans. Geosci. Remote Sens*., vol. 50, no. 7, pp. 2901-2909.

Plagge, A. M., D. Vandemark, B. Chapron, (2012) Examining the Impact of Surface Currents on Satellite Scatterometer and Altimeter Ocean Winds. *J. Atmos. Oceanic Technol.*, **29**, 1776–1793. doi: http://dx.doi.org/10.1175/JTECH-D-12-00017.1

Portabella M. (2002), “Wind Field Retrieval from Satellite Radar Systems”. PhD thesis, University of Barcelona.

Quilfen, Y., B. Chapron, A. Bentamy, J. Gourrion, T. El Fouhaily, and D. Vandemark (1999), Global ERS 1 and 2 and NSCAT observations: Upwind/crosswind and upwind/downwind measurements, *J. Geophys. Res.*, 104(C5), 11,459–11,469, doi:10.1029/1998JC900113

Quilfen, Y., B. Chapron, and D. Vandemark, (2001) The ERS scatterometer wind measurement accuracy: Evidence of seasonal and regional biases. J. Atmos. Oceanic Technol., 18, 1684–1697.

Quilfen, Y., B. Chapron, F. Collard, D. Vandemark, (2004) Relationship between ERS Scatterometer Measurement and Integrated Wind and Wave Parameters. *J. Atmos. Oceanic Technol.*, 21, 368–373.

Robinson, I.S. (2004) Measuring the oceans from space: the principles and methods of satellite oceanography, Berlin, Germany, Springer/Praxis Publishing, 669pp.

Stoffelen, A. (1998), Scatterometry. PhD thesis: University of Utrecht.

Stoffelen, A., and M. Portabella (2006), On Bayesian scatterometer wind inversion. *IEEE Trans. Geosci. Remote Sens*., vol. 44, no. 6, pp. 1523–1533.

Tran N., B. Chapron (2006), Combined wind vector and sea state impact on ocean nadir-viewing Ku- and C-band radar cross-sections. *Sensors*, 6(3), 193-207

Tran N., B. Chapron Bertrand, D. Vandemark (2007), Effect of long waves on Ku-band ocean radar backscatter at low incidence angles using TRMM and altimeter data. *IEEE Geoscience and Remote Sensing Letters*, 4(4), 542-546.

Wentz, F. J., and D. K. Smith (1999), A model function for the ocean-normalized radar cross section at 14 GHz derived from NSCAT observations. *J. Geophys. Res.*, vol. 104, no. C5, pp. 11 499–11 514.

Wentz, F. J., and M. H. Freilich (1998), Finalizing the NSCAT-1 model and progress toward NSCAT-2 in *Proceedings of the NASA Scatterometer Science Symposium*, p. 61-63, Jet Propul. Lab., Pasadena,Calif.